Ensemble Kalman Filter Analyses of Internal Rear-Flank Downdraft Momentum Surges within the 18 May 2010 Dumas, Texas Supercell

Patrick S. Skinner[1], Christopher C. Weiss[1], Louis J. Wicker[2], Corey K. Potvin[2] and David C. Dowell[3]

[1]Texas Tech University, [2]NOAA/National Severe Storms Laboratory, [3]NOAA/Earth System Research Laboratory

Motivation

- Platforms participating in the second Verification of the Origins of Rotation in Tornadoes Experiment (VORTEX2) (Wurman et al. 2012) observed a series of four internal rear-flank downdraft (RFD) momentum surges over a 15-minute period from 2250 – 2305 UTC (Figs. 1, 2).
- RFD surges were found to coincide with the development and decay of a low-level mesocyclone (Fig. 2) and qualitatively appear to be driven by a downward-directed vertical perturbation pressure gradient force (VPPGF) (Skinner et al. 2013).
- In order to undertake a quantitative analysis of RFD surge forcing and origin, a series of data assimilation experiments using an ensemble Kalman filter (EnKF) have been performed.

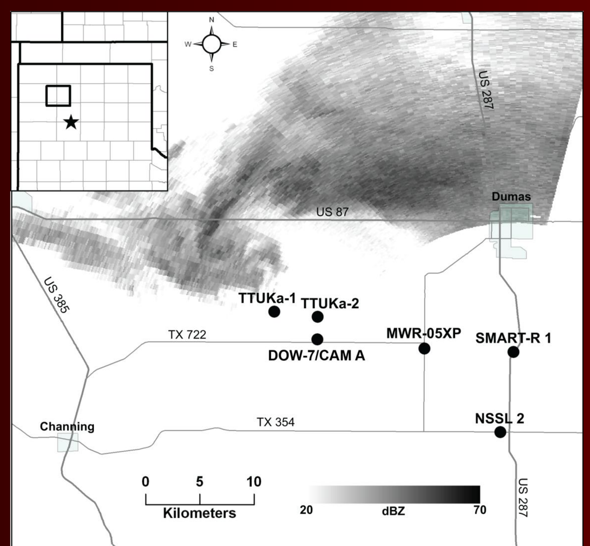

Figure 1. Locations of select VORTEX2 assets at 2300 UTC. SMART-R 0.8° elevation angle radar reflectivity at 2257:13 UTC is overlain. The star in the inset denotes the approximate position of the KAMA WSR-88D.

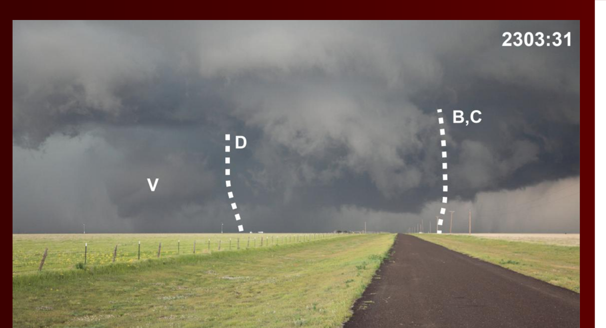

Figure 2. CAM A photograph of the Dumas supercell. Estimated position of internal RFD surge gust fronts are denoted by dashed lines and wall cloud associated with low-level mesocyclone is labeled "V".

Methodology

- Ensemble square root filter used with NCOMMAS numerical model.
- Homogeneous environment based on VORTEX2 mobile sounding (NSSL 2 in Fig. 1).
- Ensemble of 48 members run on a 100 x 100 x 20 km domain with 500 m horizontal grid spacing and a stretched vertical grid with 80 levels (100 – 700 m spacing.
- Three microphysical parameterizations were employed to account for uncertainty in the near-surface thermodynamic environment. Results from the Ziegler variable density (ZVD) scheme (Mansell et al 2010) are presented here.
- Radial velocity data from DOW-7 and SMART-R 1 as well as radial velocity and radar reflectivity data from the KAMA WSR-88D are assimilated every two minutes from 2220 – 2308 UTC (Fig. 3).
- DOW and SMART-R data are objectively analyzed to a 1-km grid using a two-pass Barnes scheme (Majcen et al. 2008) and KAMA data are analyzed to a 2-km grid using a Cressman scheme.
- Sinusoidal perturbations to the initial wind profile and additive noise (Dowell and Wicker 2009) are used to maintain ensemble spread.
- As the EnKF pressure field will contain large errors (Tong and Xue 2005), the three-dimensional perturbation pressure field is retrieved from the ensemble mean wind and thermodynamic fields.
- Retrieval technique is described by Potvin and Wicker (2013) and is based on techniques of Hane et al. (1982) and Liou et al. (2003).

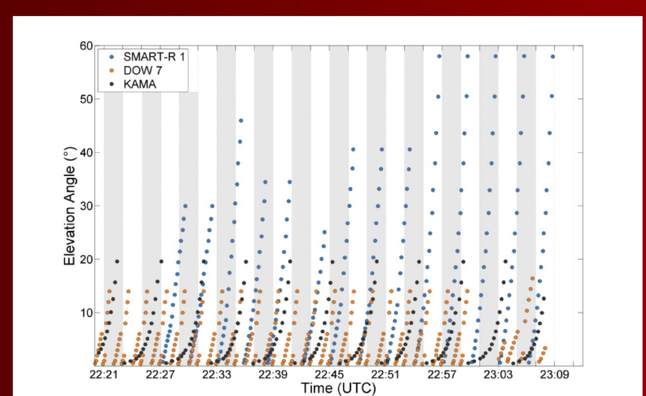

Figure 3. Time series of elevation angles used in data assimilation. Assimilation windows are denoted by alternating shaded columns.

EnKF Analyses

- All EnKF analyses produce an internal RFD momentum surge at a similar time and location as independent observations (Fig. 4) (Skinner et al. 2013).
- RFD and RFD surge perturbations of density potential temperature in ZVD experiments are most similar to observations of the Dumas supercell (Weiss et al. 2012; Skinner et al. 2013) (Fig. 4).
- Highest near-surface wind speeds occur behind leading edge of RFD surge GF and cyclonic low-level vorticity maximum occurs at the intersection of the RFD surge and primary RFD gust fronts (Fig. 4).
- Retrieved pressure and EnKF ensemble mean microphysical analyses used to calculate terms in the vertical momentum equation:

$$\underbrace{\frac{\partial w}{\partial t}}_{Figs.\_5a-c} = \underbrace{-C_p\bar{\theta}\frac{\partial \pi'}{\partial z}}_{Figs.\_5d-f} + \underbrace{B}_{Figs.\_5g-i}$$

- Upward acceleration along RFD surge GF due to VPPGF (Fig. 5).
- Downward buoyant acceleration occurs throughout RFD and RFD surge and provides "background" downward-acceleration (Fig. 5).
- The VPPGF is separated into estimated contributions of buoyancy and vertical perturbation pressure gradient using:

$$\underbrace{-C_p\bar{\theta}\frac{\partial \pi'}{\partial z}}_{Figs.\_5d-f} \propto \underbrace{-C_p\bar{\theta}\frac{\partial \pi'_d}{\partial z}}_{Figs.\_6d-f} + \underbrace{C_p\bar{\theta}\frac{\partial^2 B}{\partial z^2}}_{Figs.\_6a-c}$$

- Structure of internal RFD surge and GF primarily determined by the dynamic contribution to the VPPGF.

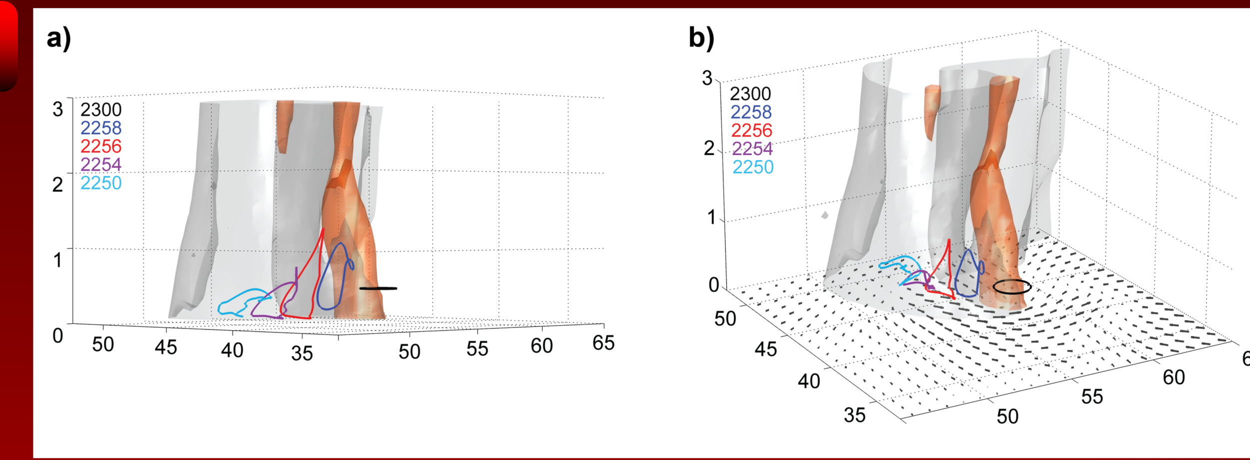

Figure 7. Color-coded location of a material circuit initialized at 2300 UTC at an altitude of 0.467 km within the RFD surge at five different times. The viewing perspectives are from the (a) southwest at an elevation angle of 0° and (b) south-southwest at an elevation angle of 20°. Ensemble mean isosurfaces of 40 dBZ simulated reflectivity and 0.02 s^{-1} vertical vorticity are plotted in gray and orange, respectively, and 2300 UTC wind vectors at 0.05 km are underlain in (b). The vertical axis has been stretched by a factor of 4 for clarity.

Material Circuit Analysis

- 10000 backward trajectories comprising a circular, 1-km radius material circuit centered over the RFD surge at 2300 UTC are calculated over a 10-minute period (Figs. 7, 8).
- Trajectories are calculated using a 1-s time step and fourth order Runge-Kutta method with linear interpolation in time and trilinear interpolation in space.
- All trajectories within the material circuit reside near the surface (<500 m) behind the FFGF at 2250 (Figs. 7, 8).
- The circuit rotates cyclonically around low-level mesocyclone (Fig. 8) with trajectories along the leading edge of the circuit experiencing larger vertical excursions (Figs. 7, 9).
- Horizontal PPGF responsible for changes in direction and wind speed of trajectories and dynamic VPPGF primarily responsibly for changes in vertical velocity (Figs. 9, 10).
- ***Which comes first, the low-level mesocyclone or the RFD surge?***

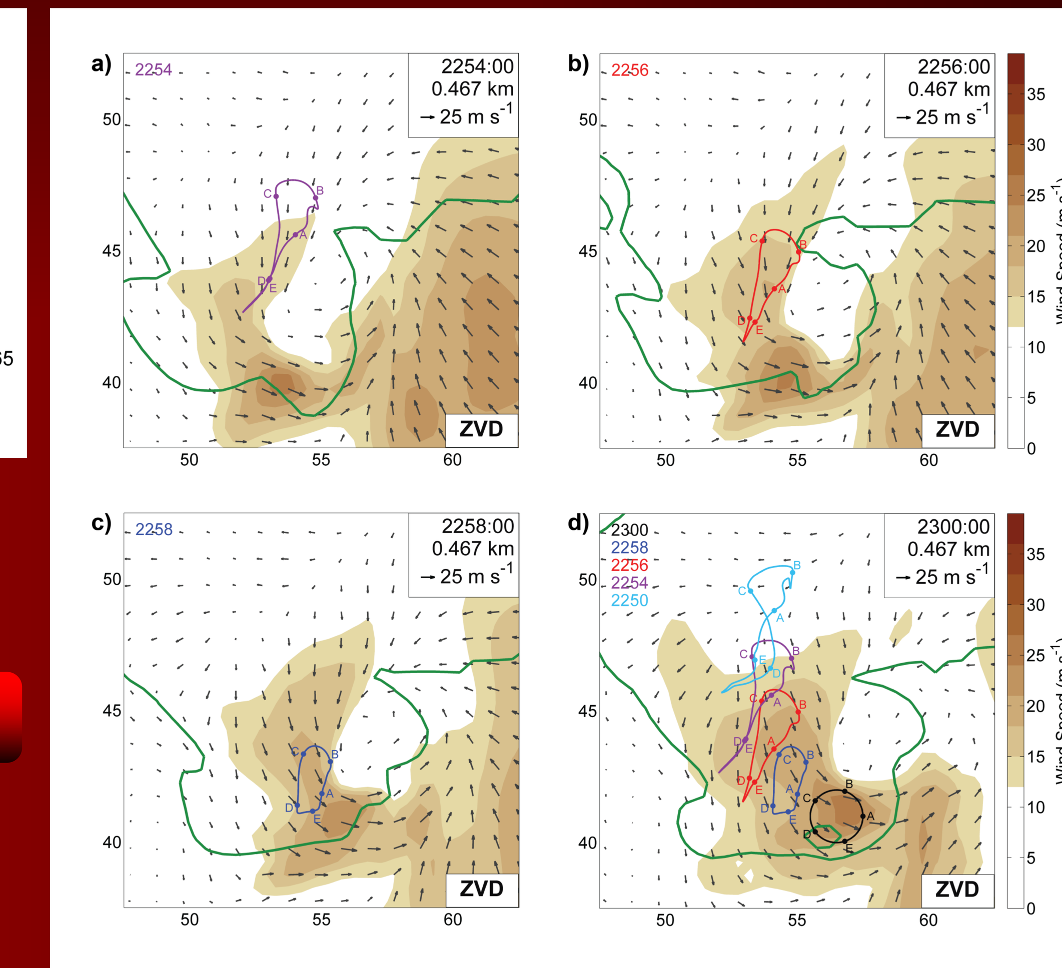

Figure 8. Horizontal location of the material circuit at (a) 2254, (b) 2256, (c) 2258, and (d) 2300 UTC. Wind speed contours, wind vectors, and reflectivity contour as in Fig. 4 and plotted at a height of 0.467 km. Location of material circuit at five times included in (d) with every 2000th trajectory denoted with letters "A" -"E".

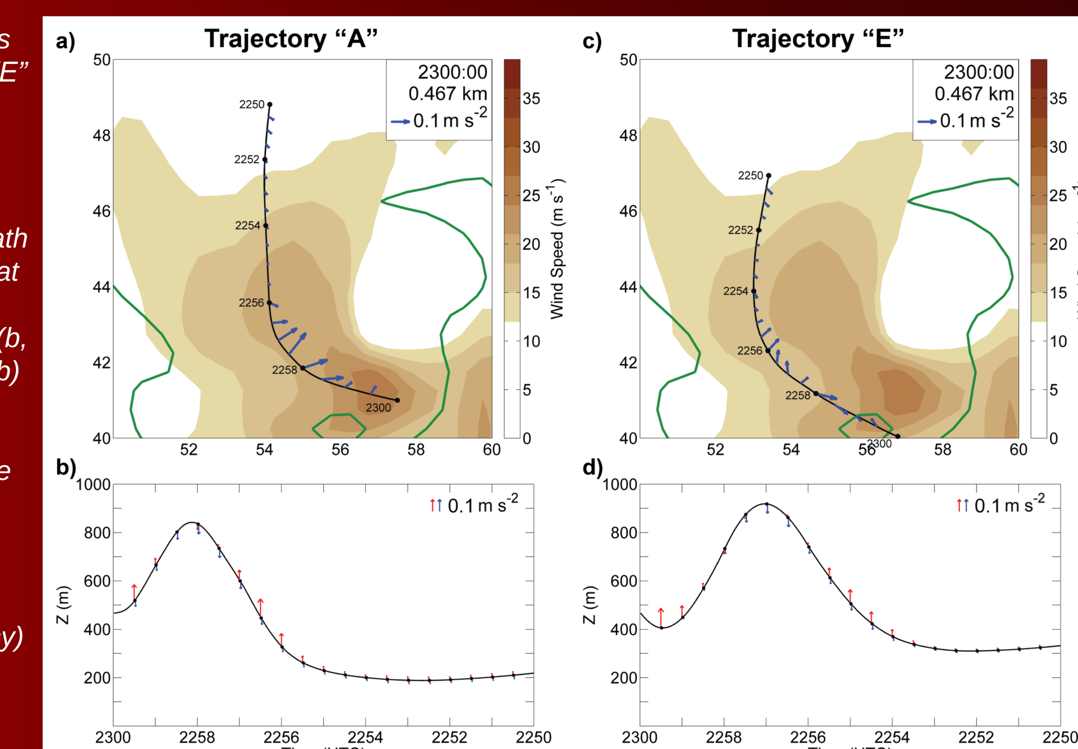

►Figure 9. (a, c) Paths of trajectories "A" and "E" as denoted in Fig. 8. Horizontal pressure gradient acceleration vectors are plotted in blue along trajectory path and trajectory position at select times is labeled. Contours as in Fig. 8. (b, d) Time-height plot of (b) trajectory "A" and (d) trajectory "E". Vertical acceleration vectors are plotted every 30 s with red(blue) vectors denoting vertical perturbation pressure gradient force(buoyancy) acceleration.

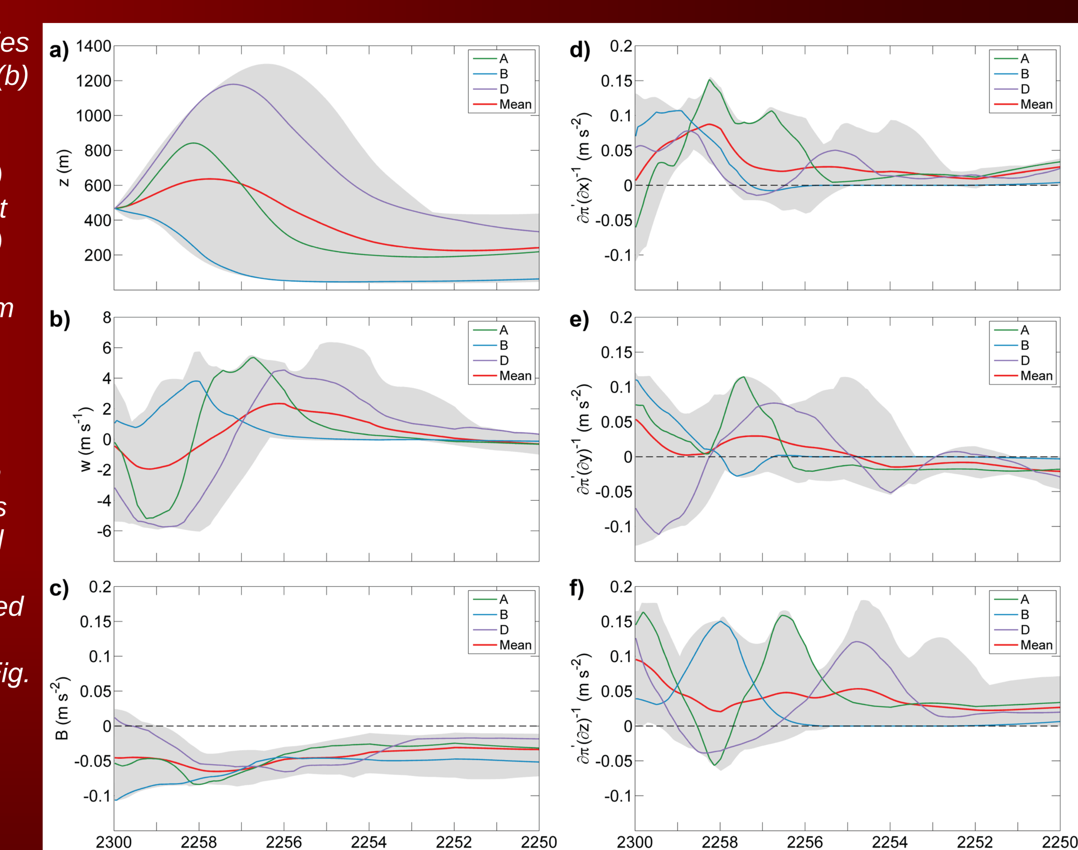

►Figure 10. Time-series plots of (a) height (m), (b) vertical velocity (m s^{-1}), (c) buoyancy acceleration (m s^{-2}), (d) zonal pressure gradient acceleration (m s^{-2}), (e) meridional pressure gradient acceleration (m s^{-2}), and (f) vertical pressure gradient acceleration (m s^{-2}). Shaded region represents the range in values of all trajectories comprising the material circuit, the mean trajectory value is plotted in red, and trajectories "A", "B", and "D" from Fig. 8 are plotted in green, blue, and purple, respectively.

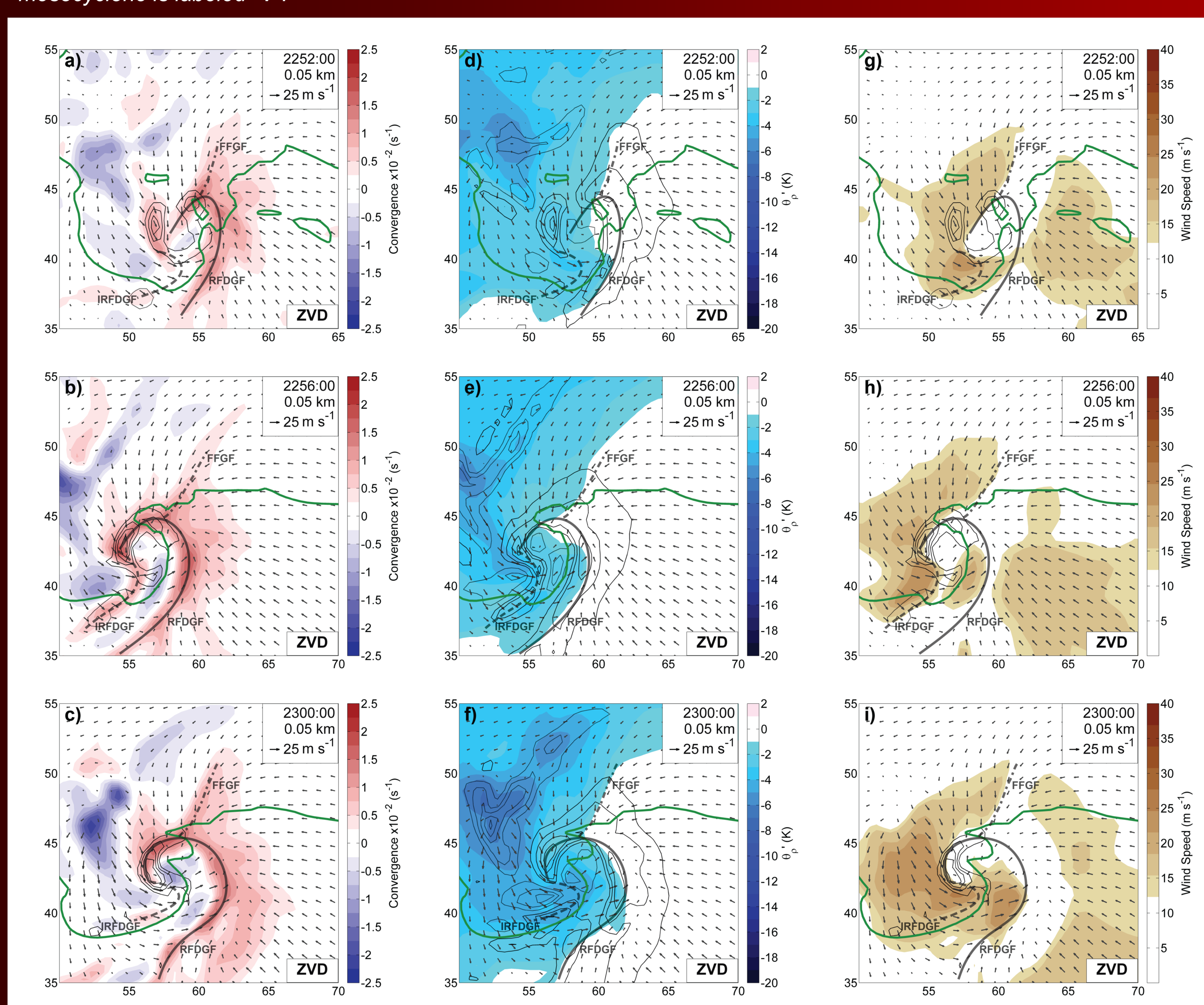

Figure 4. Ensemble mean analyses of (a-c) convergence (s^{-1}), (d-f) density potential temperature (K), and (g-i) wind speed (m s^{-1}) at the lowest vertical level (0.05 km). Wind vectors at 0.05 km are overlain as well as the simulated 20 dBZ radar reflectivity contour (thick green line) and contours of (a-c, g-i) vertical vorticity (s^{-1}) or (d-f) vertical velocity (m s^{-1}) at a height of 0.576 km. Vertical vorticity is contoured every 0.05 s^{-1} for magnitudes greater than 0.1 s^{-1} and vertical velocity is contoured every 2 m s^{-1} with negative values indicated by dashed contours. Subjectively analyzed positions of the forward-flank gust front (FFGF), RFD gust front (RFDGF), and internal RFD surge gust front (IRFDGF) are indicated by stippled, solid, and dashed lines, respectively.

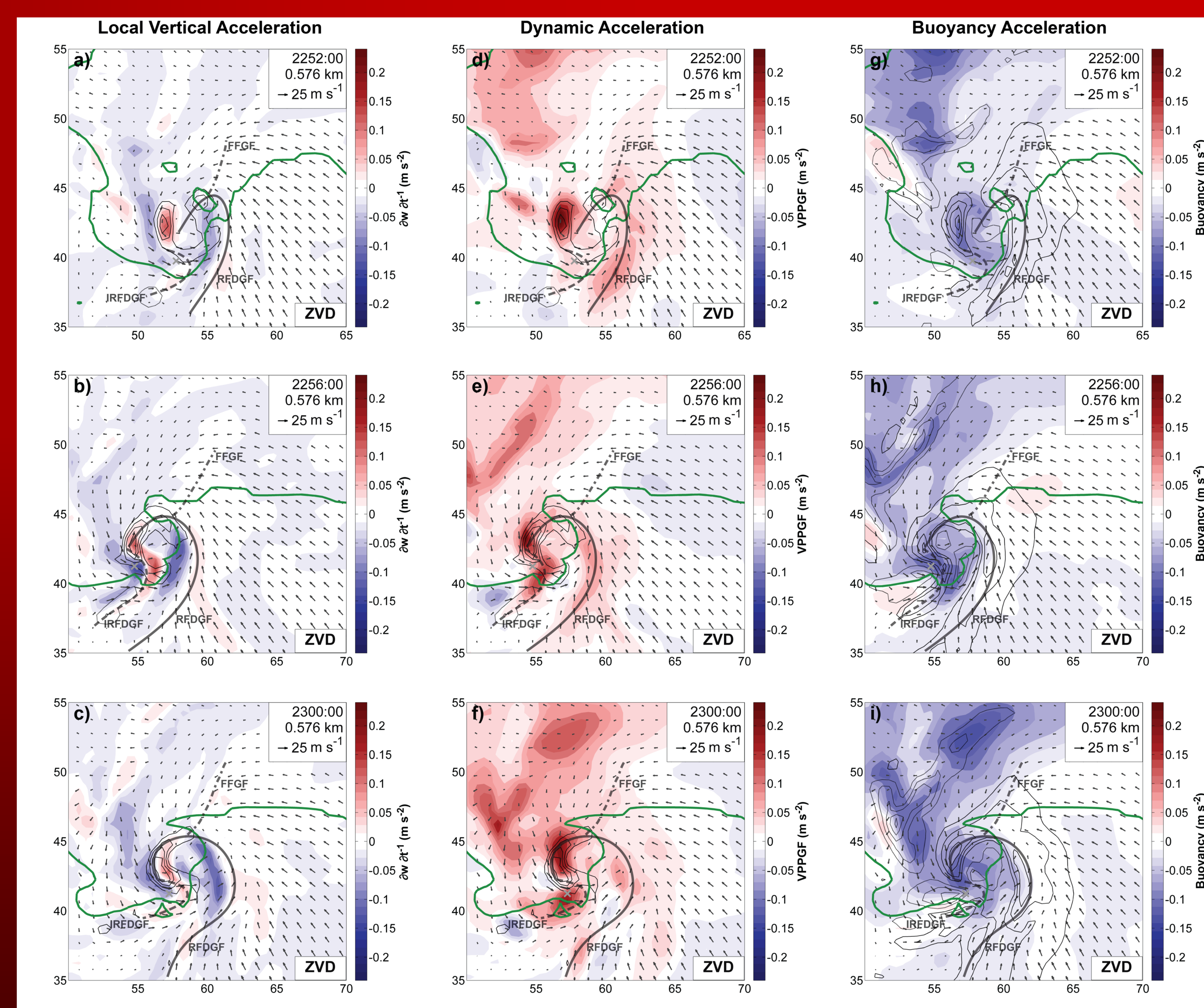

Figure 5. Contours of (a-c) local vertical acceleration (m s^{-2}), (d-f) vertical perturbation pressure gradient acceleration (m s^{-2}), and (g-i) buoyant acceleration (m s^{-2}) at 0.576 km retrieved from the ensemble mean analyses. Vertical vorticity(vertical velocity) at 0.576 km contoured as in Fig. 4 in panels a-f(g-i). Other information as in Fig. 4 except that wind vectors and simulated reflectivity contours are at a height of 0.576 km and gray "X" denotes the location of maximum wind speed at 0.05 km.

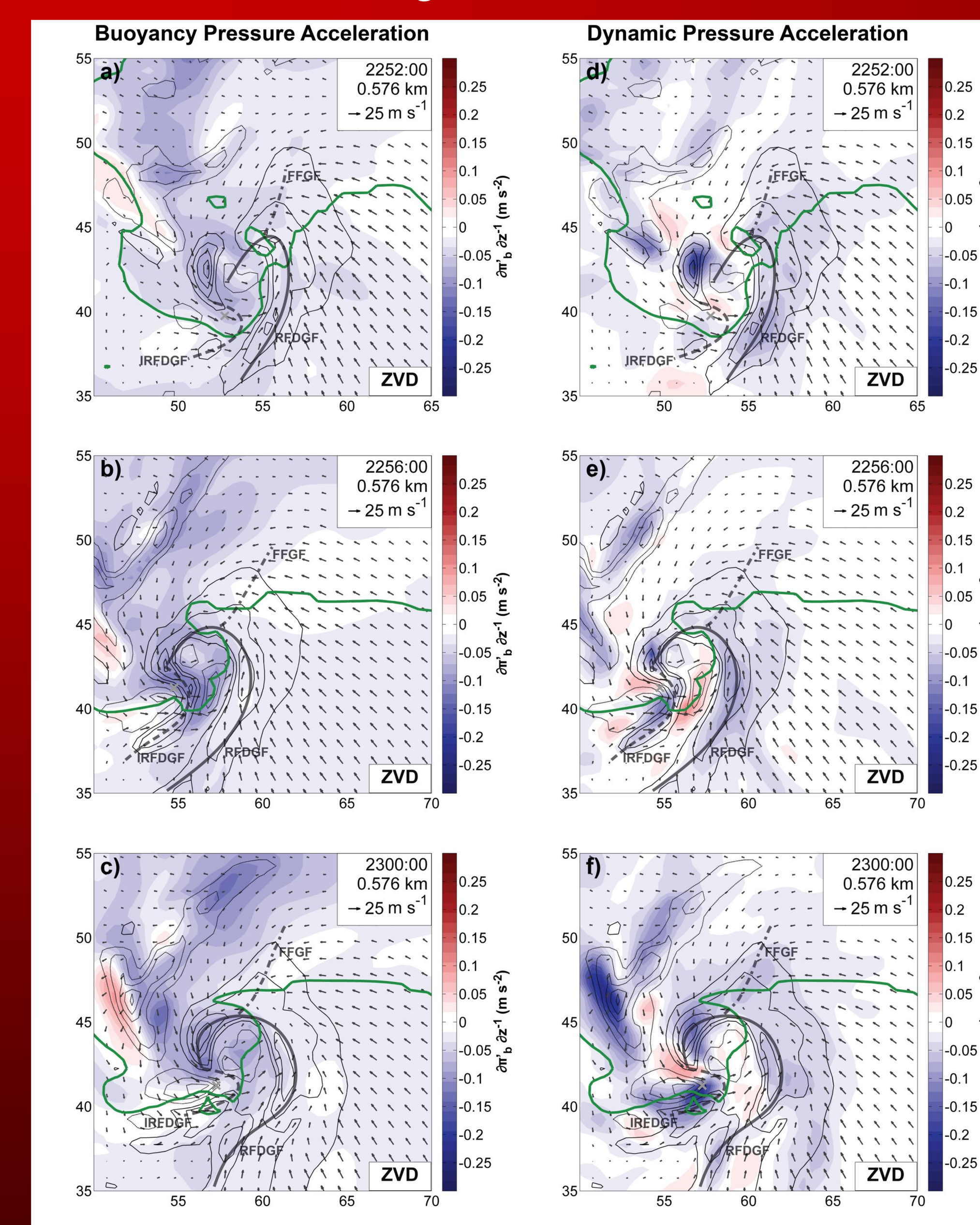

Figure 6. Qualitative estimates of (a-c) the buoyant contribution to the vertical perturbation pressure gradient acceleration (Fig. 5d-5f) and (d-f) the dynamic contribution to the vertical perturbation pressure gradient acceleration at 0.576 km. Note that the color bar has been reversed from Fig. 5, so upward acceleration is indicated by negative values (perturbation pressure decreasing with height). All other information is as in Fig. 5.

Acknowledgements

This study was supported by National Science Foundation Grant AGS-0964088 and computing support was provided by NSSL/FRDD. We wish to thank Dr. Josh Wurman, Dr. Karen Kosiba, and Dr. Michael Biggerstaff for collecting and making available DOW and SMART-R data, which was generously hosted by NCAR /EOL under sponsorship of the National Science Foundation. We are also grateful for many helpful conversations with Dr. Jim Marquis and Tony Reinhart and for the dedication of all VORTEX2 participants. References can be provided upon request.

***Corresponding Author Address: Patrick Skinner, Texas Tech University**
National Wind Institute, Box 41023 Lubbock, TX 79409
patrick.skinner@ttu.edu